Stationary, oscillating or drifting mantle-driven geomagnetic flux patches?

Hagay Amit,[1,2] Julien Aubert,[3] and Gauthier Hulot[1]

[1] The impact of the heterogeneous lower mantle on the geomagnetic field is under debate, especially the question of whether high-latitude intense geomagnetic flux patches currently observed at the core surface are stationary, oscillating, or drifting on longer time scales. While the correlation between the location of these patches with that of similar patches found in the time-averaged paleomagnetic field may suggest stationary behavior, their variability over archaeomagnetic time scales together with their weaker signature in the average paleomagnetic field relative to the present geomagnetic field precludes such a scenario. Here we use numerical dynamos with an imposed heat flux boundary condition based on lower mantle tomography to study the behavior of such intense magnetic flux patches. We design an algorithm to detect centers of intense flux patches and track their time evolution. We find that the time-dependent nature of those patches comprises oscillatory motion about statistically preferred locations imposed by mantle control, with episodic drift from one preferred location to the other corresponding to an azimuthal migration of fluid downwelling structures that concentrate surface magnetic flux. This statistical behavior provides a possible explanation for both the observed variability of high-latitude patches on the archaeomagnetic time scale and the similar locations of the current patches and the weaker patches seen in the paleomagnetic field. Our simulations also show that the patches exhibit more time dependence and less coherency in the southern hemisphere, leading to a weaker time-averaged patch signature in that hemisphere.

1. Introduction

[2] The geomagnetic field is generated by flows in an electrically conductive fluid at Earth's outer core in a process known as the geodynamo. Over the past decade, many studies investigated mantle control on the geodynamo [*Glatzmaier et al.*, 1999; *Bloxham*, 2002; *Olson and Christensen*, 2002; *Christensen and Olson*, 2003; *Aubert et al.*, 2007; *Gubbins et al.*, 2007; *Willis et al.*, 2007; *Amit et al.*, 2008]. Increasing evidence suggests that the geodynamo is strongly influenced by the heterogeneous lower mantle [e.g., *Aubert et al.*, 2008a]. The mechanism by which thermal mantle heterogeneity can produce non-axisymmetric geomagnetic features is rather well-understood. Lower mantle thermal heterogeneity and thermal core-mantle coupling correspond to lateral variations in the heat flux across the core-mantle boundary that

induce thermal winds at the top of the core [*Bloxham and Gubbins*, 1987]. The poloidal flow associated with this thermal wind then concentrates the magnetic field at some preferred locations. Somewhat surprisingly however, the pattern of the time-average magnetic field driven by a given thermal mantle heterogeneity can vary significantly in numerical models, depending on the chosen model parameters [*Olson and Christensen*, 2002; *Takahashi et al.*, 2008].

[3] A related issue is that of the nature of the time dependence of the mantle-controlled magnetic field. Two extreme types of behavior have been found so far. In highly supercritical numerical dynamos with comparable thermal and magnetic diffusivities and no buoyancy sources or sinks, magnetic field structures are too mobile for mantle control to be detected in a snapshot. In those dynamos mantle signature in the field can only arise robustly when considering long-term time-averages over several magnetic diffusion times [*Bloxham*, 2002; *Olson and Christensen*, 2002]. A more detailed examination of the same type of models by *Aubert et al.* [2007] nevertheless revealed that some mantle control signature could be detected in maps of the core flow (rather than of the field) averaged over intermediate time scales equivalent to the historical time period. Another extreme type of behavior can be found in slightly supercritical numerical dynamos with magnetic diffusivity an order of magnitude

[1]Equipe de Géomagnétisme, Institut de Physique du Globe de Paris, Université Paris-Diderot, INSU, CNRS, Paris, France.
[2]Laboratoire de Planétologie et de Géodynamique, UMR 6112, Université de Nantes, CNRS, Nantes Atlantiques Universités, Nantes, France.
[3]Equipe de Dynamique des Systèmes Géologiques, Institut de Physique du Globe de Paris, Université Paris-Diderot, INSU, CNRS, Paris, France.

Table 1. Parameters Used in the Dynamo Simulations[a]

Case	q^*	Ra	Ra/Ra_c	E	Pm	Rm
T0lr	0.5	6×10^5	2.96	3×10^{-4}	3	90
T0	0.5	1×10^6	4.94	3×10^{-4}	3	125
T0hr	0.5	4×10^6	19.74	3×10^{-4}	3	303
T0hq	0.75	1×10^6	4.94	3×10^{-4}	3	126

[a]Heat flux based Rayleigh (Ra), Ekman (E) and magnetic Prandtl (Pm) numbers (for definitions, see *Olson and Christensen* [2002]). The magnitude of the heat flux anomaly imposed on the outer boundary q^* is defined as the ratio of peak-to-peak to twice the mean heat flux. The level of convective supercriticality is given by Ra/Ra_c. In all cases the Prandtl number is set to $Pr = 1$. Also given the magnetic Reynolds number $Rm = Pm\sqrt{2Ek}$ calculated based on Ek, the kinetic energy density in the volume of the shell. All cases have imposed tomographic outer boundary conditions. Case $T0$ is from *Amit et al.* [2008].

smaller than thermal diffusivity, and a volumetric buoyancy source. In those dynamos the magnetic field can become locked to the boundary heterogeneities when those and the underlying convection have comparable length-scales, and a strong thermal diffusion is used to allow the boundary anomalies to penetrate and organize the flow in the shell. In such dynamos a snapshot can thus already contain a clear mantle control signature [*Gubbins et al.*, 2007; *Willis et al.*, 2007].

[4] All those studies thus shed contradicting lights on the long-term behavior and possible persistence of the well-known high-latitude intense magnetic flux patches found in the modern and historical geomagnetic field [*Jackson et al.*, 2000; *Hulot et al.*, 2002], the signature of which is also found in some time-average paleomagnetic field models [*Johnson and Constable*, 1995, 1997; *Kelly and Gubbins*, 1997], but in a weak and not necessarily robust way [*Carlut and Courtillot*, 1998; *Khokhlov et al.*, 2001, 2006]. These non-axisymmetric features typically appear near the edge of the tangent cylinder, most likely due to flow convergence at these latitudes. In the present study we therefore focus on the dynamics of these outer boundary magnetic structures and further investigate whether mantle control results in stationary, oscillating or drifting magnetic flux patches. More specifically, we wish to characterize the attraction mechanism by which the mantle heterogeneity may control such non-axisymmetric field features. A similar study of time-dependent mantle-driven intense magnetic flux patches has already been performed by *Bloxham* [2002] using a numerical dynamo model with an imposed spherical harmonic degree and order two (Y_2^2) boundary condition. Here however we examine the same problem in greater detail.

[5] The paper is organized as follows. In section 2 we introduce our method. We use numerical dynamos with imposed heat flux pattern on the outer boundary based on the multiharmonic lower mantle tomography model of *Masters et al.* [2000]. We investigate dynamo models with varying control parameters, because as already pointed out, dynamo properties, including the time-average magnetic field, are parameter-dependent. We then introduce an algorithm to analyze long time series of snapshots for identifying and tracking the time evolution of intense magnetic flux patches. This type of analysis provides a quantitative and objective way of evaluating the nature of time dependence in the mantle-driven magnetic field. We report the results of our analysis for each dynamo model and investigate the physical

mechanisms responsible for the time dependence of the intense patches in section 3. Finally, section 4 discusses the possible geophysical implications of our results.

2. Method

[6] We use self-consistent 3D numerical dynamos in a spherical shell with heterogeneous heat flux imposed on the outer boundary based on the lower mantle tomography model of *Masters et al.* [2000] (for control parameters, see Table 1; for details on the method, see *Aubert et al.* [2007]). With these boundary conditions, the Rayleigh number is defined based on the mean outer boundary heat flux q_0 by $Ra = \alpha g_0 q_0 D^4 / k\kappa\nu$, where α is thermal expansivity, g_0 gravitational acceleration, D shell thickness, k thermal conductivity, κ thermal diffusivity and ν kinematic viscosity [e.g., *Olson and Christensen*, 2002]. We use highly supercritical models with $Ra/Ra_c \sim 3$–20 (where Ra_c is the critical value for the onset of non-magnetic convection). The thermal and magnetic diffusivities are of the same order of magnitude, and no buoyancy sources or sinks are assigned. The models were initialized using random fields and analysis commenced after all fields reached statistical equilibrium. The models yield dipole-dominated surface magnetic fields with strong time dependence, as in previous studies [e.g., *Olson et al.*, 1999].

[7] Because the magnetic Reynolds number in numerical dynamos is of the correct Earth-like order of magnitude, the details of magnetic induction are assumed to be reasonably modeled. We therefore consider the simulation output time in units of magnetic diffusion times converted into equivalent Earth years, so the dimensionalized time is obtained by factoring the simulation time by $\frac{1}{Pm}\frac{D^2}{\lambda}$ where Pm is the magnetic Prandtl number, $D = 2200$ km is the outer core shell thickness and $\lambda = 1$ m^2/s is the core's magnetic diffusivity [*Secco and Schloessin*, 1989]. Each simulation was run for several magnetic diffusion times. In case $T0$ (see Table 1) with a Rayleigh number about five times critical the simulation was run for 360 kyr. Snapshots of the radial magnetic field B_r on the outer boundary were taken every 530 years or so. Although significant changes may occur from one snapshot to the next, these are usually close enough in time to allow associating and tracking intense magnetic flux patches. In the larger Ra number case $T0hr$ (about 20 times critical) the simulation was run for 450 kyr, in the smaller Ra number case $T0lr$ (about three times critical) the simulation was run for 1130 kyr, and in the larger boundary anomaly q^* case $T0hq$ the simulation was run for 405 kyr. In all cases the time between successive snapshots, on the order of several centuries, was again chosen to allow the tracking of intense flux patches.

[8] Regions of intense patches are identified by searching grid points where the absolute radial field is larger than a critical threshold $|B_r(\phi, \theta)| > f_b|Br(\phi, \theta)|_{\max}$. This condition is defined with respect to the instantaneous field. We set $f_b = 0.6$ for all cases. We found that overall the sensitivity of our results to f_b is very weak. Figure 1 shows an example of a B_r snapshot from case $T0$ (top) and the extreme points identified according to the above criterion. In the next step, we perform an algorithm based on the principles of the classical connected component labeling method previously used in geophysics for detecting mantle plumes in a mantle convec-
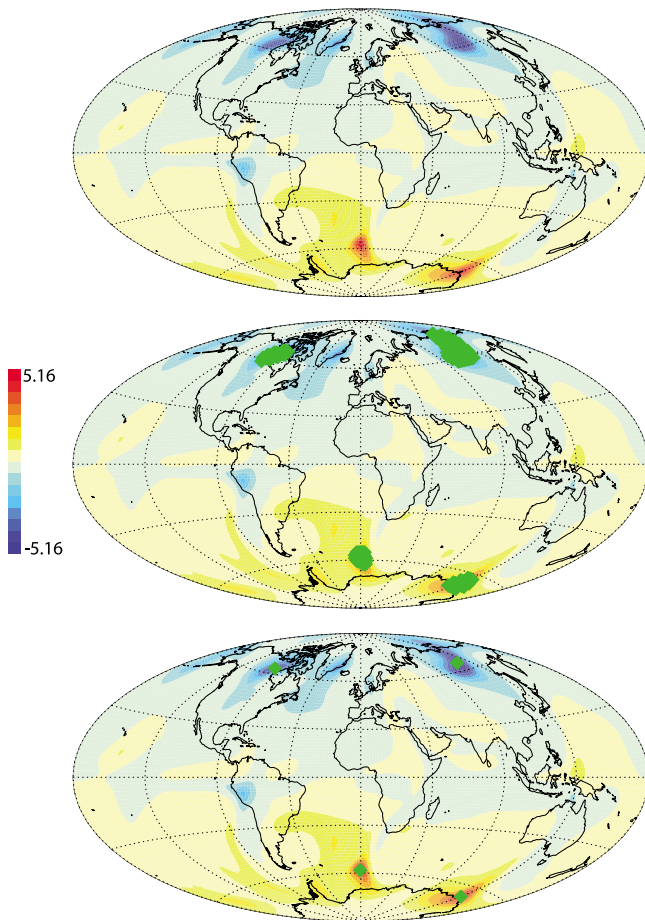
Figure 1. (top) Radial magnetic field on the outer boundary of case $T0$ in an arbitrary snapshot at time $t = 388.0$ kyr, (middle) with diamonds at extreme intense grid points and (bottom) with diamonds at centers of mass. The field is given in units of $\sqrt{\rho\mu_0\lambda\Omega}$, where ρ is density, μ_0 is magnetic permeability of free space, λ is magnetic diffusivity and Ω is rotation rate.

tion simulation [*Labrosse*, 2002]. The identified extreme points are grouped based on the spherical distance between one extreme point to another. Once all extreme points are assigned to a given group, a center of mass is calculated for each group. These centers of mass represent centers of intense patches (Figure 1, bottom). When applying the same algorithm for a higher Ra number (case $T0hr$), the identification of patches works very well for this smaller scale dynamo as well (Figure 2), although the small-scales make the tracking of patches more difficult.

[9] In each case the algorithm was implemented with the same value of f_b for all snapshots. For obtaining the locations of the patches of the time-average fields, however, we used different fractional values denoted by $\langle f_b \rangle$ (Table 2) in order to adjust to the different length-scales and different zonal components in the time-average maps. The time-average radial magnetic field of case $T0$ and the centers of mass representing the centers of intense patches are shown in Figure 3 (top right). The non-axisymmetric structure in this map, most notably the four high-latitude intense normal polarity patches (two in each hemisphere), will be used as

a reference state for the time-dependent mantle-controlled field. The time-average fields of cases $T0lr$, $T0hr$ and $T0hq$ are also shown in Figure 3.

[10] Two patches in consecutive snapshots are labeled as the same patch if the spherical distance between them is smaller than a critical value. Because the temporal behavior relies on the typical velocity of each model, for this critical threshold we use relative values that correspond to an azimuthal distance $\delta^c = \omega^e \, \Delta t Rm^e/Rm$, where $\omega^e \sim 0.2°$/yr is an upper bound longitudinal drift value based on inferred low-latitude fast drifting geomagnetic features and $Rm^e \sim 500$ is an estimated magnetic Reynolds number for Earth's core [*Bloxham and Jackson*, 1991], Δt is the time step, and Rm is each model's magnetic Reynolds number (Table 1). Our choices of ω^e and Rm^e are based on geophysical inferences. Although these may be debated, they allow consistent comparison between the dynamo models.

[11] Movies of the surface radial magnetic fields (see Br_movie_case.gif in the auxiliary material) are rich in different types of patches behavior, including drift, formation, dispersion, merge and split.[1] For an objective and simplified analysis, we plot time series of the coordinates of the centers of mass of the patches (e.g., Figure 4 for case $T0$). As time progresses in these time series, each new color represents a new patch. For a given color, positive/negative trends correspond to eastward/westward patch drift in the longitude curves, or northward/southward in the latitude curves. Combining these time series and the movies allows objective tracking of the time evolution of the intense patches.

[12] Time series such as Figure 4 can be analyzed synthetically for integrated quantitative measures of the behavior of the intense flux patches. First, we calculate the time-derivatives of their longitudes in order to distinguish between semi-stationary periods termed 'St' (characterized by small time-derivatives) and drifts (characterized by large time-derivatives), with the threshold being $\delta^c/2\Delta t = \omega^e \, Rm^e/2Rm$. We also distinguish between integrated amounts of time of eastward and westward drifts (denoted by 'Ea' and 'We'). The absolute RMS drift rates (here without distinguishing east or west) is also reported. Second, we quantify the time dependence of the patches by their average and maximum lifetimes τ_a and τ_m, and the probability p for each patch to be found in the vicinity (15° longitudinal distance) of one of the patches identified in the time-averaged field (Figure 3). All quantities are given for each hemisphere separately. The analysis of the time series is summarized in Table 3. Sensitivity tests based on half simulation times show fast convergence with a confidence level of up to ±1%–2% in the values of the synthetic analysis.

3. Results

[13] We first describe the intense magnetic field patches identified in the time-average B_r maps (Figure 3). The coordinates of the intense patches in the studied cases are given in Table 2. The time-average magnetic field exhibits strong sensitivity to the dynamo control parameters. Only in case $T0$ is the dominant Y_2^2 pattern in the tomographic model expressed by two intense patches in each hemisphere. In the

---

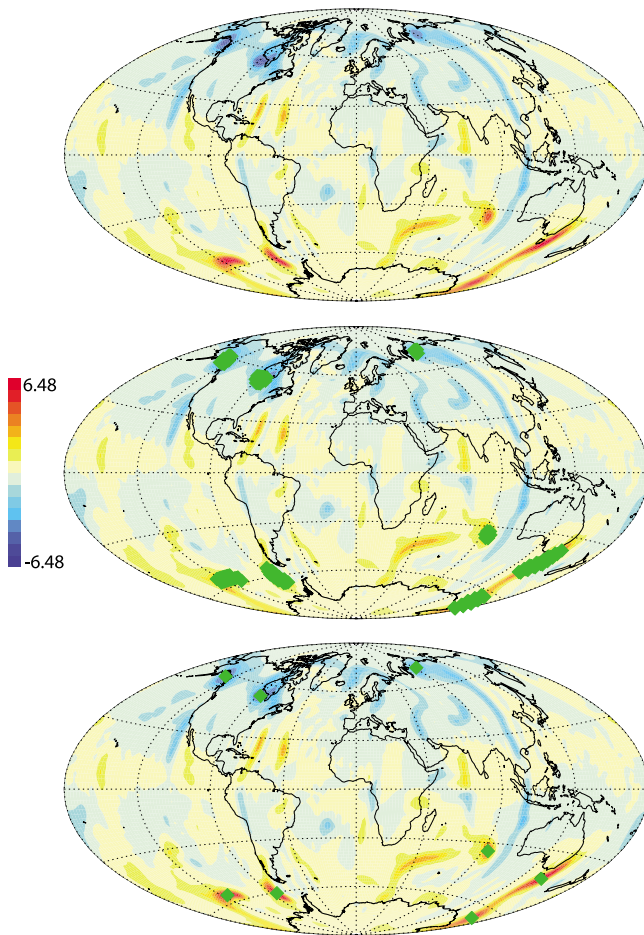[1]Auxiliary materials are available in the HTML. doi:10.1029/2009JB006542.

Figure 2. Same as Figure 1 for case *T0hr* at time *t* = 455.8 kyr.

other cases only one patch or none (*T0lr*) is detected in the southern hemisphere, and in case *T0hq* again only one patch is detected in the northern hemisphere. The latitudes of all intense flux patches in the time-average B_r maps are just on the edge of the tangent cylinder, in the narrow range 64°–69°. In contrast, the longitudinal positions exhibit a much broader range. For example, the patch below Canada ranges between 200°E–260°E.

[14] Next we describe the time dependence of the intense flux patches. Figure 4a shows the time series of the coordinates of the centers of mass of the intense patches in the northern hemisphere in case *T0*. Latitudinal variations are small and confined to a narrow band near the edge of the tangent cylinder where the time-average patches are present. We focus on the longitudinal time dependence. The time evolution of the patches is generally composed of oscillations about either of the two time-average longitudes, with episodic drift from one preferred longitude to another.

[15] The time series in the northern hemisphere of case *T0*, together with the corresponding B_r movie (Movie S1), simplify the understanding of the time evolution of the intense flux patches. Between 360 < *t* < 385 kyr a persistent intense flux patch appears below Siberia with oscillations amplitude of about ±45°. Then this patch drifts eastward until reaching below Canada and remaining there between 400 < *t* < 425 kyr with smaller oscillations of ±25°. Later follows an eastward

drift until reaching below Siberia again at about *t* = 440 kyr. At *t* = 445 kyr the Siberian patch splits and starting from around *t* = 450 kyr a patch appears below Canada until *t* = 490 kyr with oscillations of ±35°. Then it drifts and merges with an emerging Siberian patch at *t* = 500 kyr. A new patch emerges between the two fixed longitudes below Alaska at *t* = 510 kyr, and remains there until *t* = 530 kyr. It then splits to produce a Canadian patch which between 535 < *t* < 580 kyr displays especially large oscillations of ±80°. It eventually disperses and the Siberian patch prevails between 580 < *t* < 595 kyr with small oscillations of ±25°. Then a long period of eastward drift starts in which the patch passes through Canada and reaches Siberia at *t* = 640 kyr. Then a new Canadian patch emerges and between 640 < *t* < 655 kyr both patches oscillated little, the Canadian patch by ±20° and the Siberian by ±30°. At *t* = 660 kyr a new Siberian patch emerges, drifts eastward, passes below Canada at *t* = 665 kyr, continues eastward and bounces back westward to settle in Canada between 670 < *t* < 690 kyr with small oscillations of ±20°. The Canadian patch drifts eastward until reaching Siberia at *t* = 710 kyr where it remains until the end of the simulation.

[16] Overall, intense flux patches spend more time below Canada and Siberia, the locations of the time-average non-axisymmetric magnetic field structures, than elsewhere. The duration of a semi-stationary phase ranges 15–45 kyr, but some significant oscillations of up to ±20°–±45° about the average longitude take place within such a semi-stationary period. Patches either disperse, split, merge or migrate from one preferred location to another. In the northern hemisphere of case *T0*, these drift events turn out to be more eastward than westward. The duration of the drift of a patch from Canada to Siberia or from Siberia to Canada is typically shorter than the duration of a semi-stationary phase of a patch about one of these preferred longitudes. The drift events take about 10–20 kyr, roughly twice shorter than the semi-stationary periods.

[17] Time-derivatives of the northern hemisphere longitude time series in Figure 4a allow the calculation of the relative periods of semi-stationarity, eastward and westward drifts. The results of this analysis are given in Table 3. The synthetic analysis confirms the qualitative interpretation of Figure 4a. Intense patches remain near a preferred location a comparable time to that spent drifting from one preferred location to another. Eastward drifts occur more than westward drifts in the northern hemisphere.

[18] Figure 5 shows four B_r snapshots during an eastward drift event. Starting from a semi-stationary preferred location near Canada, the patch drifts generally eastward for about 16 kyr, until reaching Siberia for the next semi-stationary

Table 2. Fractional Threshold $\langle f_b \rangle$ for Defining Extreme Points for the Time Averages and the Resulting Coordinates of the Intense Flux Patches at Each Hemisphere[a]

Case	$\langle f_b \rangle$	NH	SH
T0lr	0.95	(200.7,68.1), (115.9,68.2)	–
T0	0.55	(259.5,64.3), (113.0,67.5)	(354.1, −67.6), (143.7, −66.7)
T0hr	0.75	(248.9,64.1), (45.4,65.4)	(208.8, −66.2)
T0hq	0.6	(239.9,64.5)	(27.6, −69.0)

[a]NH/SH denote northern/southern hemisphere, respectively. Coordinates are given in longitude and latitude.
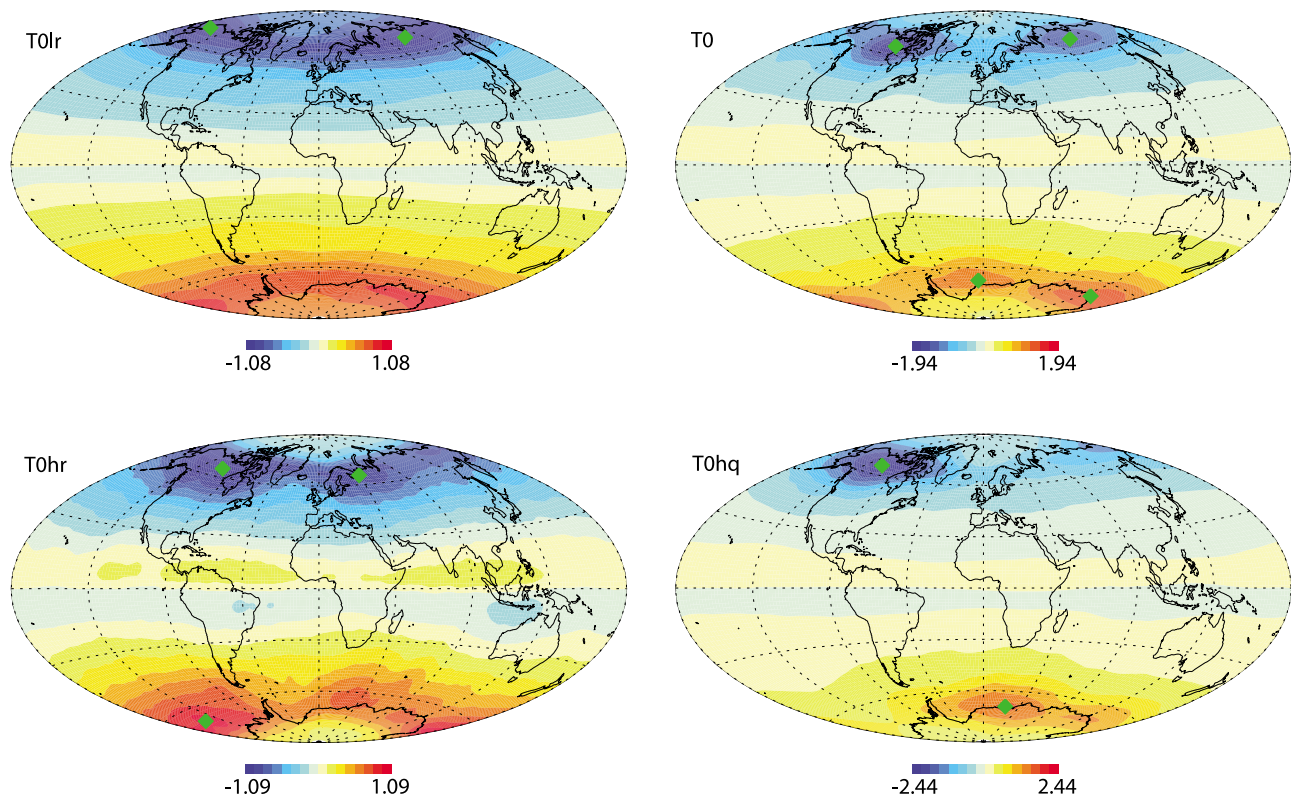
Figure 3. Time-average radial magnetic field on the outer boundary of the four cases. Diamonds mark centers of mass of intense patches. The field is given in units of $\sqrt{\rho\mu_0\lambda\Omega}$.

period. At most times along the drift event the patch is located near the edge of the tangent cylinder. Occasionally the patch splits into two patches and later regroups. During this event, the drift is about half the calculated mean rate in the northern hemisphere (Table 3), reflecting the non-monotonous nature of the drift.

[19] Next we examine the longitudinal time dependence of the intense magnetic flux patches in the southern hemisphere of case $T0$ (Figure 4b). The evolution of the patches is more time-dependent than in the northern hemisphere. Although the intense patches still spend more time at the preferred longitudes than elsewhere, they may often be found at other locations. More patches with shorter average lifetime in Figure 4b represent stronger time dependence as evident by the smaller τ_a value. In contrast to the preferred eastward drift in the northern hemisphere, the preferred drift direction in the southern hemisphere is westward (Table 3).

[20] We repeat the same analysis for the higher Ra number case $T0hr$ (not shown). The tracking is more difficult when the forcing is stronger due to the smaller scales of the magnetic field and the occasional emergence of low-latitude intense patches, some of which have a reversed polarity. The strong time dependence in this case is reflected in the much smaller τ_a and τ_m values than in case $T0$ in both hemispheres (Table 3). Despite these difficulties, some phenomena observed in case $T0$ can also be detected in case $T0hr$. The patches spend more time around Canada and Europe in the northern hemisphere and southeast Pacific in the southern hemisphere (which are the preferred locations in this case) than elsewhere. Large oscillations of ±50° about the mean longitudes are observed. Stronger time dependence in the

southern hemisphere is expressed by smaller τ_a and τ_m. In contrast, the azimuthal drifts from one preferred location to another in both hemispheres are balanced. The lower Rayleigh number case $T0lr$ is characterized by patches with short lifetime (Figure 6), especially in the southern hemisphere, as expressed by the low τ_a value in Table 3. Magnetic field locking is not observed, and the intense flux patches display little preference in their longitudinal position.

[21] We also examine the sensitivity of the mantle-driven magnetic field behavior on the boundary anomaly amplitude. In Figure 7 we show the time series in case $T0hq$ which is identical to case $T0$ except that the mantle heterogeneity is increased by 50%, i.e., $q^* = 0.75$ (Table 1). In this case intense patches in the northern hemisphere oscillate about the mean locations at most times, while dispersion and split events are less frequent (see largest τ_a value in Table 3). In contrast, in the southern hemisphere the time-average intense magnetic field patch is weaker, and often no patch is detected in the snapshots (note lower 'St' and especially τ_a and τ_m values in the southern hemisphere in Table 3). Also note that in both hemispheres the westward drift is preferred, but much more so in the southern hemisphere.

[22] Our analysis allows calculation of the probability p for a patch to be in the vicinity of a preferred location. The longitudinal distance between the time-dependent Canadian patch in the historical field of *Jackson et al.* [2000] with respect to its counterpart in the paleomagnetic field of *Kelly and Gubbins* [1997] is between 0°–25°, while with the Siberian patch the range is 10°–16°, so we arbitrarily choose 15° longitude as a critical distance for defining vicinity. The reference probability (when patches wander randomly
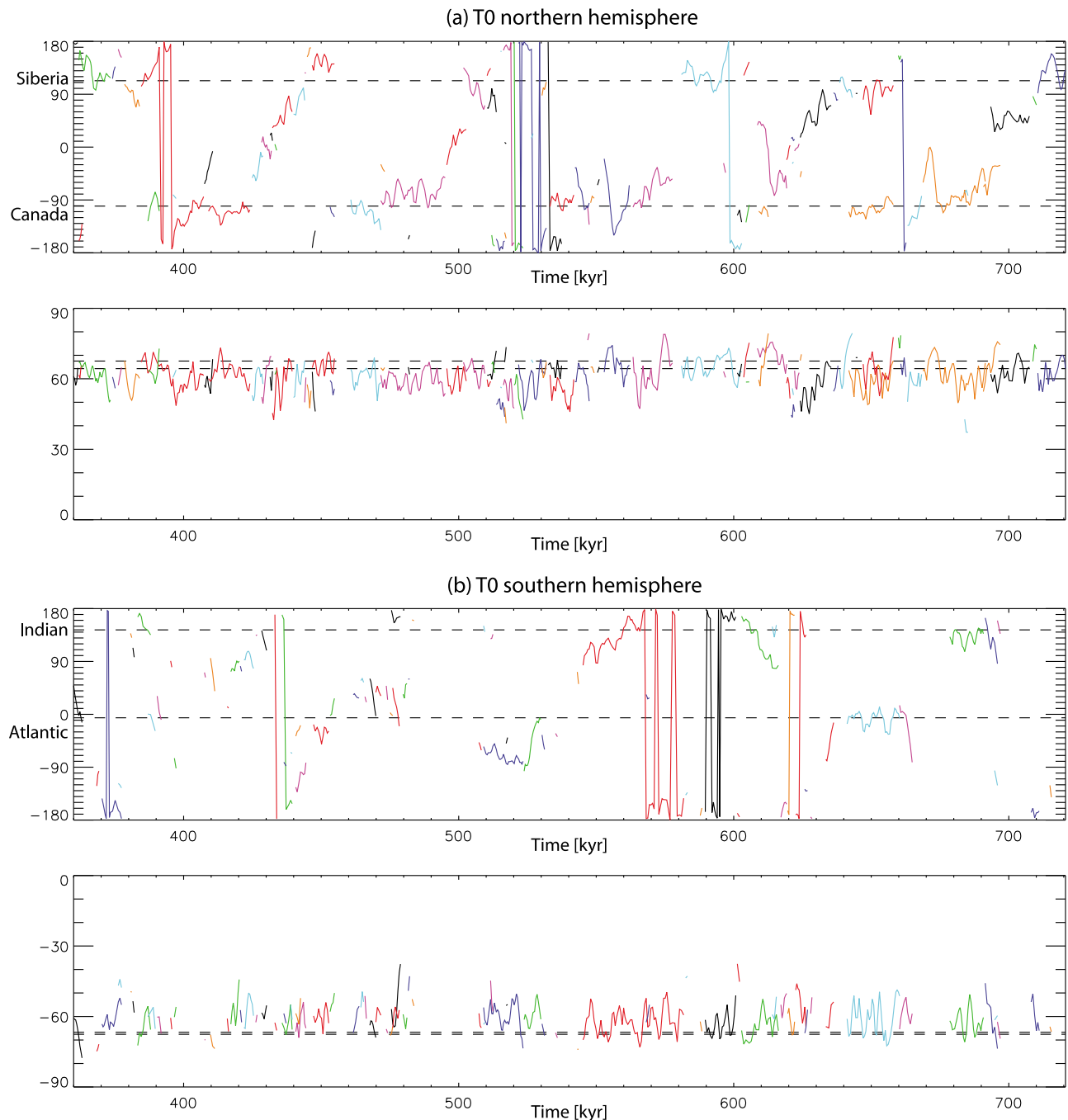
Figure 4. Time series of the (top) longitude and (bottom) latitude of the centers of mass of intense patches (distinguished by different colors) in case $T0$ in the (a) northern and (b) southern hemispheres. Coordinates units are in degrees. Dashed horizontal lines denote the coordinates of the patches identified in the time-averaged field in each hemisphere (Figure 3). As time progresses, each new color represents a new patch. For a given color, positive/negative trends correspond to eastward/westward patch drift in the longitude curves, or northward/southward in the latitude curves.

with no preferred location, as is the case for dynamos with homogeneous boundary conditions) is therefore $p_1 = 8.3\%$ for cases with one time-average patch, and $p_2 = 16.7\%$ for cases with two time-average patches. The p values in Table 3 are above these critical values for all cases. The strongest mantle control appears as expected in case $T0hq$, where $p/p_1 \simeq 2.9$ in the northern hemisphere (with one preferred location) and

$p/p_1 \simeq 2.0$ in the southern hemisphere (also with one preferred location). The weakest control is found in case $T0lr$ where $p/p_2 \simeq 1.1$ in the northern hemisphere (with two preferred locations) while there is no preferred location in the southern hemisphere.

[23] In three of the models, cases $T0$, $T0lr$ and $T0hq$, a single patch per hemisphere is often observed in the snap-

Table 3. Synthetic Analysis of Time Series[a]

Case	St	Ea	We	Ne	Rate	τ_a	τ_m	p	p/p_i
Northern Hemisphere									
T0lr	43.3	23.3	32.8	−9.5	0.024	2.52	51.5	18.3	1.10
T0	52.5	28.1	19.4	8.7	0.024	3.97	24.0	30.4	1.82
T0hr	52.9	22.1	25.0	−2.9	0.082	1.64	15.1	21.6	1.29
T0hq	53.2	22.4	24.4	−2.0	0.025	4.94	47.6	24.0	2.89
Southern Hemisphere									
T0lr	36.2	23.0	40.8	−17.8	0.025	2.12	24.2	–	–
T0	49.7	19.9	30.4	−10.5	0.024	2.46	37.3	21.6	1.29
T0hr	48.8	22.9	28.3	−5.4	0.082	1.48	11.4	9.2	1.11
T0hq	40.0	19.2	40.8	−21.6	0.026	2.31	17.4	16.5	1.99

[a]Relative integrated durations of semi-stationary events (denoted by 'St'), eastward/westward drifts (denoted by 'Ea'/'We' respectively), all in %. The net drift is defined by $Ne = Ea - We$. The threshold distinguishing semi-stationary events from drifts is $\delta^c/2\Delta t$. The RMS values of the absolute drift rates (denoted by 'Rate') are given in °/yr. The average and longest lifetimes of patches τ_a and τ_m are given in *kyr*, and the probability p for each patch to be found in the vicinity (within 15° longitude) of one of the time-average flux patches (computed as the relative time spent by all patches within those vicinities) is given in %. The probability normalized to the reference probability of being within such a vicinity by chance, taking into account the number $i = 1$ or 2 (see Table 2) of patches in the time-average field, is given by p/pi. The analysis is given for each hemisphere, with northern/southern hemispheres denoted by NH/SH, respectively.

shots. The smallest number of patches is found in case *T0hq*, in which the time-average map also contains only one patch per hemisphere. In contrast, more and smaller scale patches are observed in the large *Ra* number case *T0hr*, typically three per hemisphere. In all cases more patches per snapshot are seen in the northern hemisphere than in the southern.

[24] Our results show significant case-to-case variations in terms of drift directions. In case *T0* the preferred drift is eastward in the northern hemisphere and westward in the southern, in cases *T0lr* and *T0hq* both hemispheres have more westward drift, and in case *T0hr* the two directions are comparable. We propose that the main mechanism responsible for the drift of high-latitude intense flux patches is migration of fluid downwelling. High-latitude intense magnetic flux structures are maintained by surface convergence associated with columnar cyclones [*Olson et al.*, 1999; *Aubert et al.*, 2008b], so the flow near these patches has a large field-aligned component. This flow field relation is demonstrated globally in Figure 8 for a series of three snapshots from case *T0* (the same relations are found in the other cases as well). As can be seen in the vorticity and divergence images, centers of downwellings coincide with centers of cyclones [*Olson et al.*, 1999, 2002; *Amit and Olson*, 2004; *Amit et al.*, 2007]. Downwellings are also associated with non-axisymmetric intense magnetic field structures [*Olson and Christensen*, 2002], as can be seen in the magnetic field images, and thus the flow near these intense patches has a large component parallel to B_r-contours and produces little magnetic advection. We further demonstrate the significant flow component along B_r-contours of an intense flux patch in a close-up of such a region in Figure 9. The drift of the intense patches is therefore caused by migration of the downwelling structures rather than magnetic flux advection by the surface
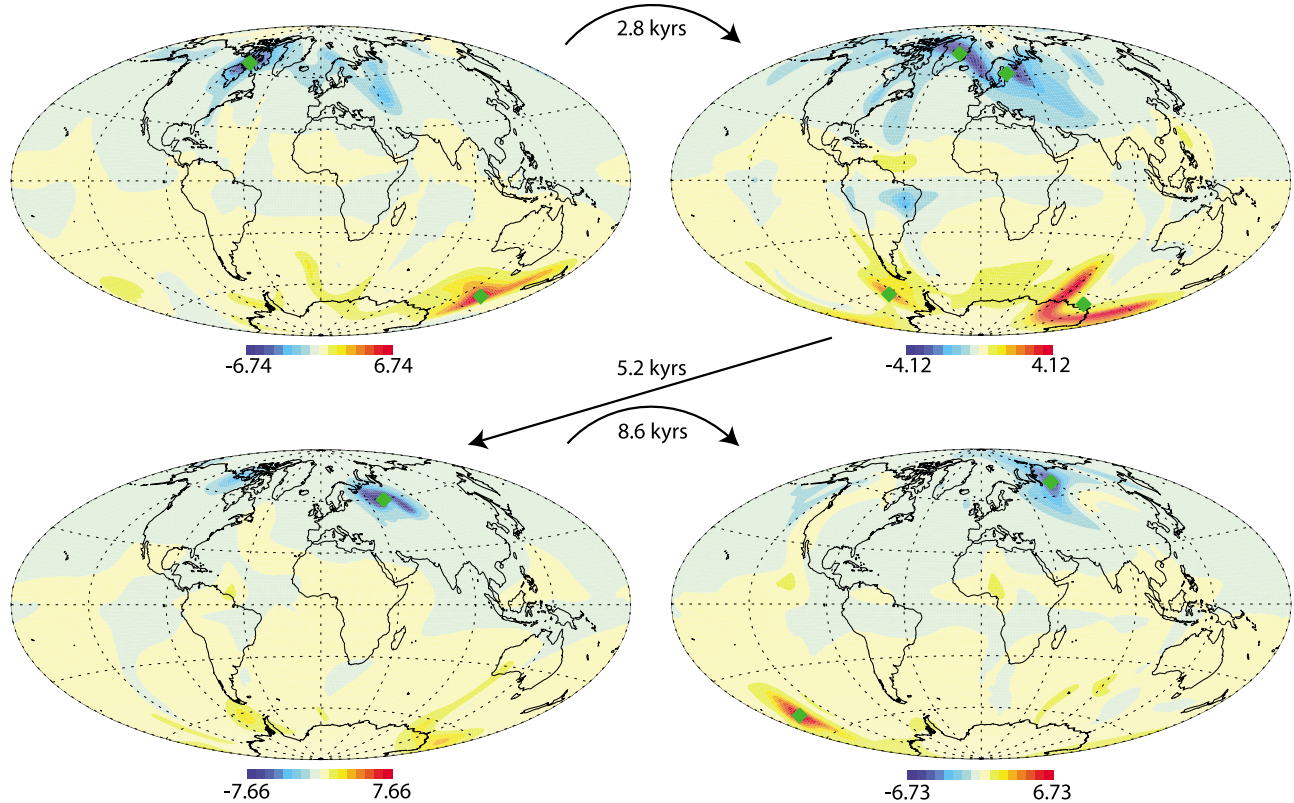

Figure 5. Eastward drift of a patch from a preferred location near Canada starting at time $t = 692.1$ kyr to a preferred location near Siberia in case *T0*. The field is given in units of $\sqrt{\rho\mu_0\lambda\Omega}$.
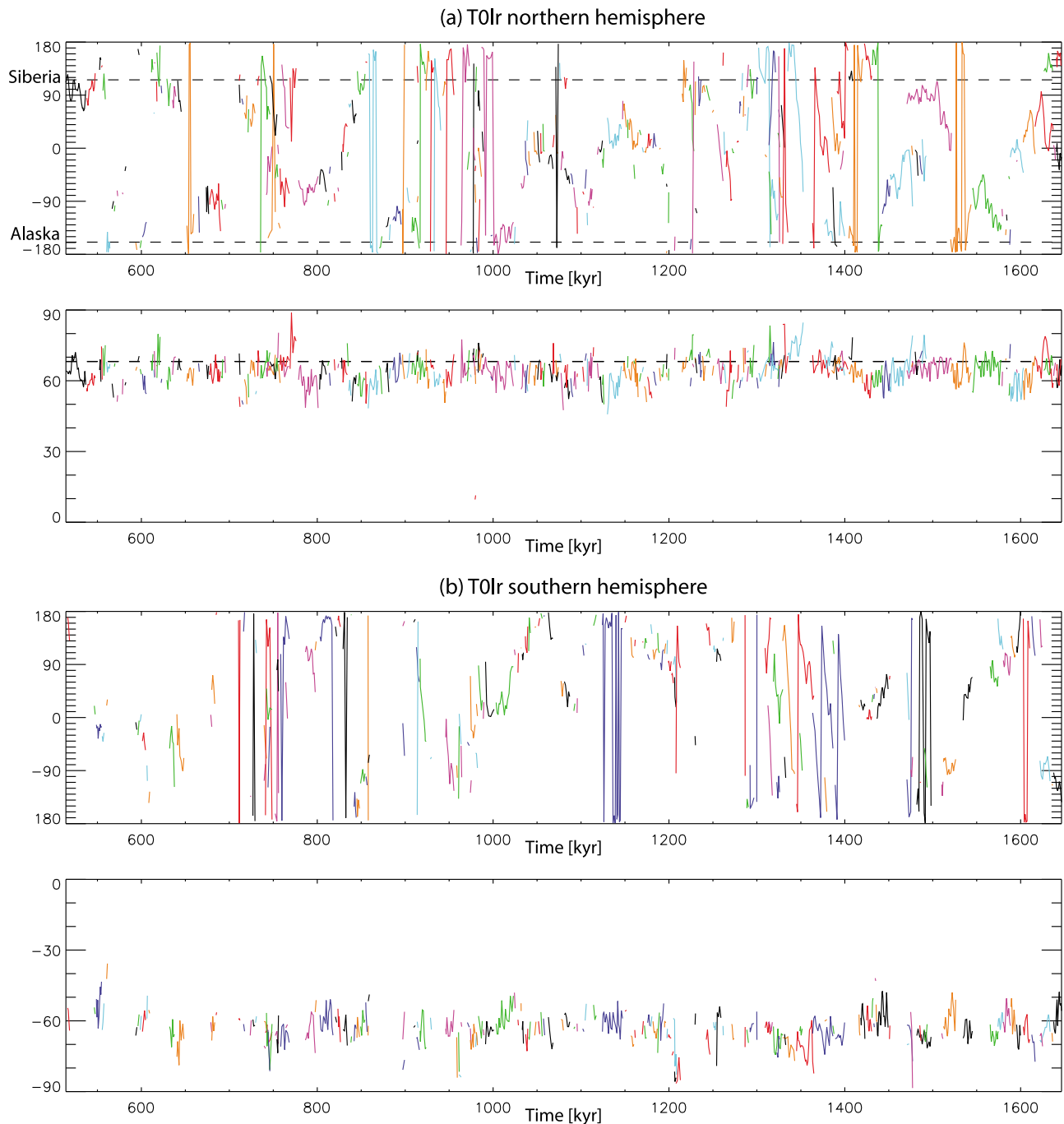
Figure 6. Same as Figure 4 for case *T0lr*.

flow. As a cyclone migrates, the magnetic patch in the old location fades, either due to shear flow, magnetic diffusion or advection. Once the cyclone settles in a new location, surface convergence concentrates a new magnetic flux patch.

[25] In addition, the time-average mantle-driven flow pattern may play a role in some secondary drifting effects. Recall the net preferred drift $Ne = Ea - We$ measuring the difference between eastward and westward drifts, which we computed for each case and in each hemisphere (Table 3). Common to all cases is the north-south dichotomy in Ne, with more negative (i.e. more westward) values in the southern hemisphere. This dichotomy can be associated with the

mantle-driven time-average zonal velocity profile. In numerical dynamos with homogeneous boundary conditions, this profile is perfectly symmetric about the equator, with westward polar vortices, eastward flow at high-latitudes outside the tangent cylinder, and weak flow at low and middle latitudes [*Aubert*, 2005; *Amit and Olson*, 2006]. In all cases considered in this study, however, the zonal part of the imposed heat flux heterogeneity contains north-south asymmetry resulting in a similar asymmetry in the zonal thermal wind, with more westward drift in the southern hemisphere (as had also been noted by *Amit and Olson* [2006]). As can be seen in Figure 10, surface zonal flows outside the tangent

(a) T0hq northern hemisphere
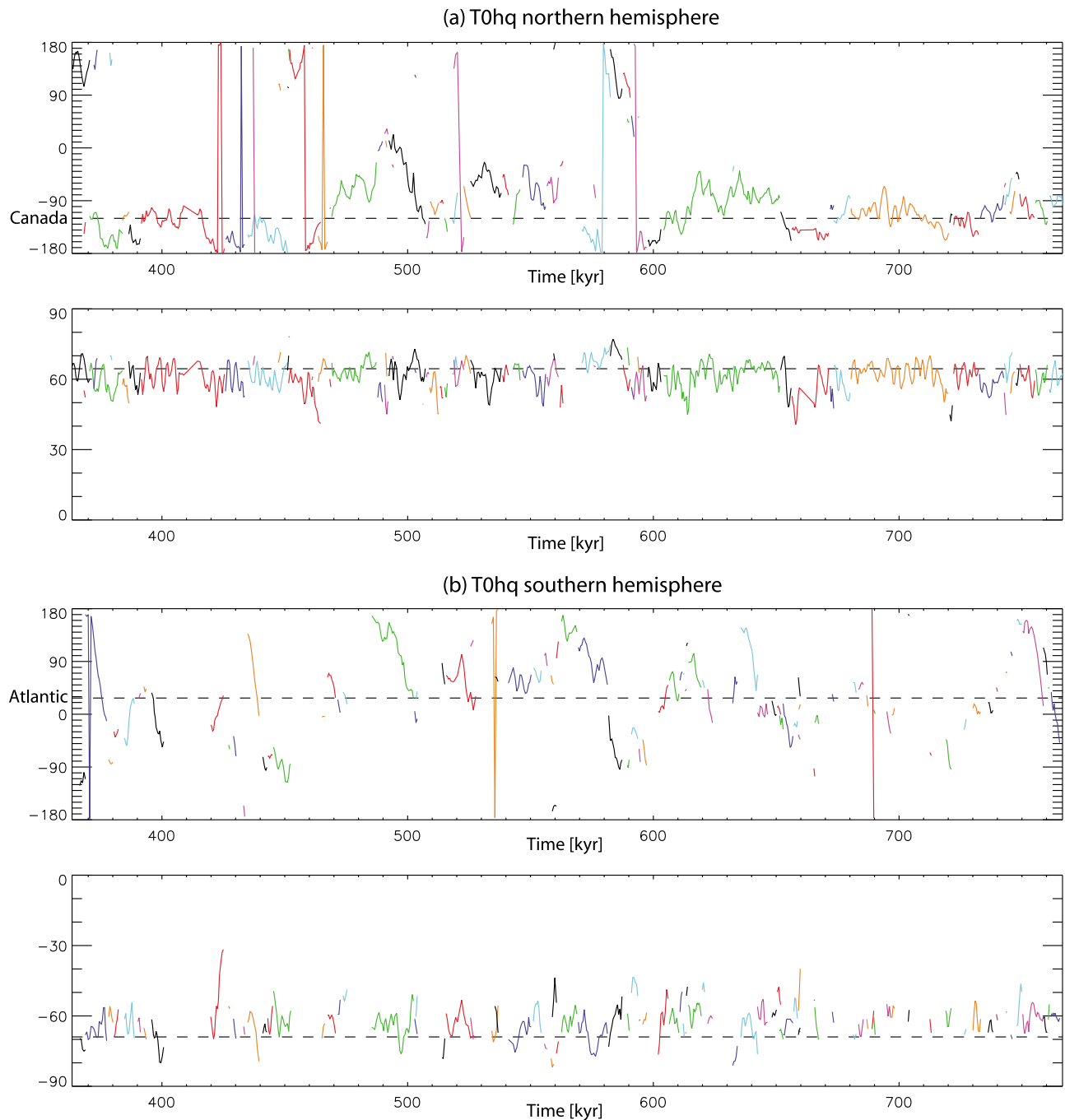

(b) T0hq southern hemisphere

Figure 7. Same as Figure 4 for case *T0hq*.

cylinder are eastward from high-latitudes down to nearly the equator in the northern hemisphere. In contrast, eastward zonal flows are confined to a narrow high-latitude band in the southern hemisphere with westward zonal flows prevailing at midlatitudes. Magnetic advection may therefore play the secondary role of dismantling magnetic flux patches by meridional shear after a cyclone has migrated, and the mantle-driven zonal flow could provide more of this meridional shear in the southern hemisphere.

[26] The mantle-driven time-average zonal velocity profile may also provide a possible explanation for the stronger time dependence in the southern hemisphere in all cases, expressed

by shorter semi-stationary periods, smaller average patch lifetime and smaller probability to be near a time-average location. Time-average mantle-driven meridional shear acting on magnetic field structures in the southern hemisphere splits and disperses these structures. This may be the reason for the weaker time-average magnetic flux patches in the southern hemisphere with respect to the northern time-average intense patches (Figure 3).

[27] Finally, note that in both hemispheres the average patch lifetime ranges $\tau_a \sim$ 1–5 kyr in all cases, while the oldest patches reach $\tau_m \sim$ 10–50 kyr. While some patches have a lifetime of only several vortex turnover times, others live as
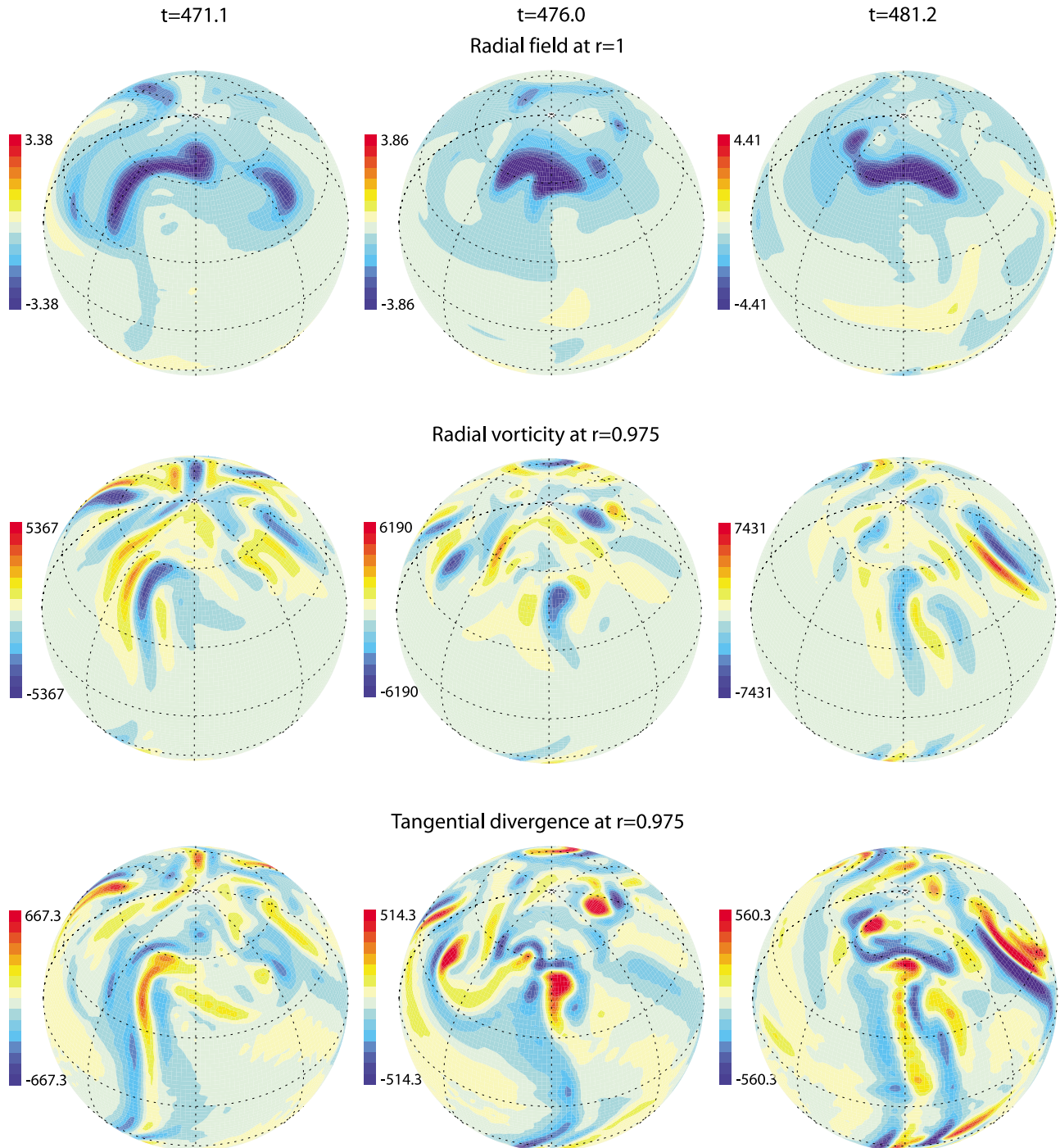
Figure 8. Field-flow relationship for three different snapshots in case $T0$. (top) The radial field B_r is given in units of $\sqrt{\rho \mu_0 \lambda \Omega}$, (middle) the radial vorticity ω_r, and (bottom) tangential divergence of the flow $\nabla_h \cdot \vec{u_h}$ are in units of ν/D^2 where ν in the kinematic viscosity and D is the shell thickness, time is in units of kyr. Red/blue radial vorticities correspond to cyclonic/anticyclonic flow in the northern hemisphere (vice versa in the southern hemisphere); red/blue tangential divergences correspond to upwelling/downwelling. Each column corresponds to a different snapshot. The maps are centered at longitude $90W$.
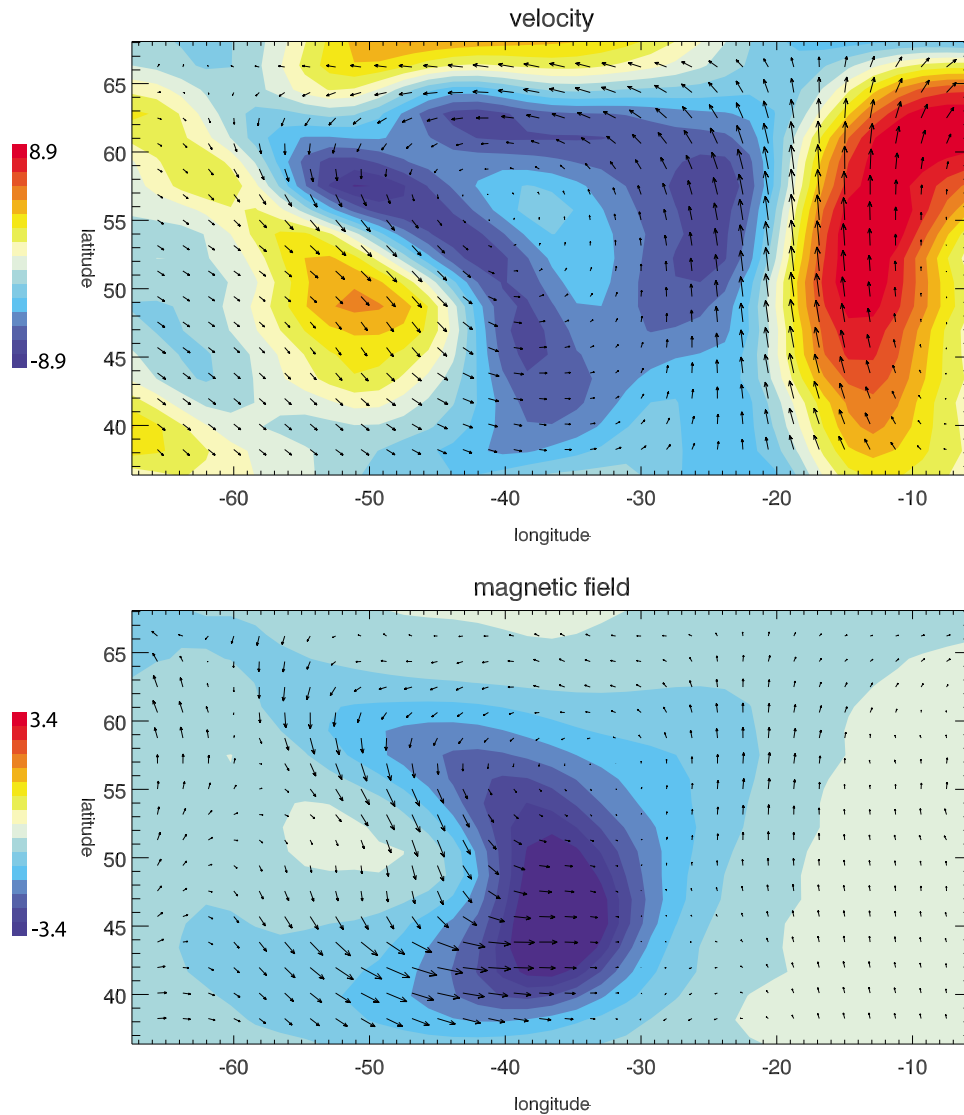
Figure 9. Close-up of (top) velocity and (bottom) magnetic field at the top of the free stream of a snapshot from case $T0$ at $t = 471.1$ (Figure 8, left). Colors represent radial components; arrows indicate tangential components. The field is given in units of $\sqrt{\rho\mu_0\lambda\Omega}$; the flow is given in units of ν/D. Maximum tangential flow is 134.5, maximum tangential field is 2.8.

long as a magnetic diffusion time. This disparity is a further demonstration of the vigorous dynamics of the high-latitude intense patches in highly supercritical dynamos.

4. Discussion

[28] Due to computational limitations, and just like all accessible numerical dynamo simulations, our simulations operate in a parametric regime still very far from that of the Earth's core [*Glatzmaier*, 2002]. In addition, the models can exhibit a broad range of behaviors and are very sensitive to small changes in the control parameters. Any inference from those simulations should thus be taken with great care. However, probably the most important model parameter for studying the kinematics of intense magnetic flux patches, as we did in this study, is the magnetic Reynolds number, which represents the ratio of magnetic advection to diffusion. In our models, Rm is comparable to that of Earth's core. It is

therefore quite reasonable to assume that the analysis in this study could reflect, at least qualitatively, the behavior of geomagnetic flux patches on various timescales.

[29] Our results would then suggest that some locking of the magnetic field with respect to the mantle can occur in the form of intense magnetic flux patches oscillating (significantly) about a preferred location, but also episodically disappearing, reappearing or drifting from one preferred location to another. These drift events are caused by azimuthal propagation of fluid downwelling structures. Our numerical dynamo models are within the commonly used parameter regime of highly supercritical Ra numbers [e.g., *Christensen et al.*, 1999] in which vigorous convection results in chaotic dynamics and strong secular variation. This choice is supported by parametric studies which suggest high supercriticality in Earth's outer core [*Christensen and Aubert*, 2006]. It is important to note that this is a very different choice from that of using slightly supercritical ($Ra/Ra_c < 1.5$)
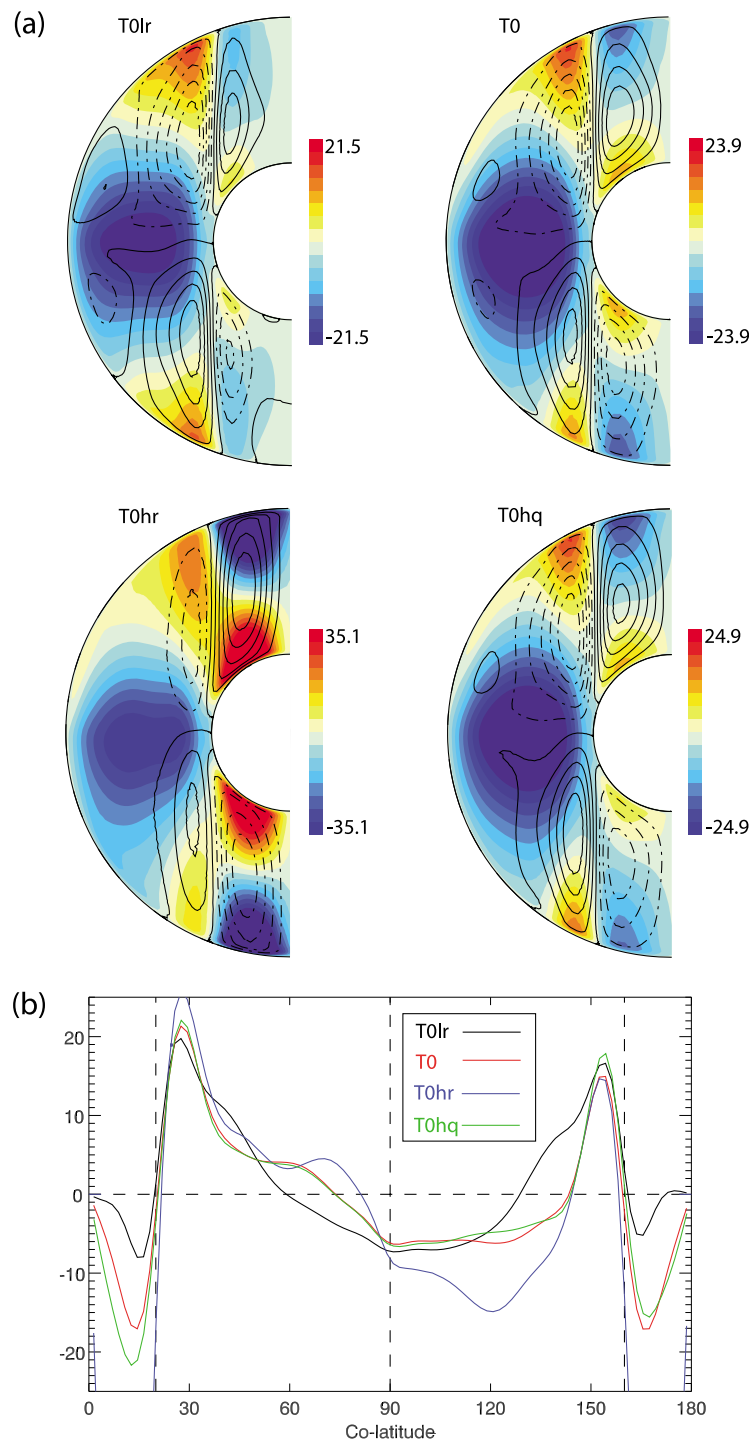
Figure 10. Time-average zonal profiles of azimuthal velocities (a) in the shell and (b) at the top of the free stream for each case considered in this study. In Figure 10a, red/blue denote eastward/westward flow; contours represent meridional circulation (solid/dashed denote anticlockwise/clockwise flow). The flow is given in units of ν/D.

conditions, in which the time dependence is very weak and the magnetic field at a snapshot is very similar to the long-term time-average leading to locked dynamos [*Gubbins et al.*, 2007; *Willis et al.*, 2007]. Interestingly a different type of model was recently introduced by *Sreenivasan and Gubbins* [2008] with imposed Y_2^2 temperature boundary condition, and

in which partial locking with some mobility was also found. They obtained locked magnetic fields using more realistic parameters than *Willis et al.* [2007], i.e. higher Rayleigh numbers and order one magnetic Prandtl numbers, by assigning volumetric buoyancy sinks that correspond to compositionally dominated convection. These sinks produce

vigorous convection at depth but weaker convection or even stable stratification at the top of the shell. The resulting magnetic flux patches in those models are more mobile (i.e. less locked) than those of *Willis et al.* [2007]. *Sreenivasan and Gubbins* [2008] argued that this time dependence of the patches is in agreement with the geomagnetic observations. Those results therefore agree with our findings that an intermittent regime of oscillatory motion about preferred locations with episodic drift from one location to another could indeed apply to the Earth's dynamo.

[30] Our quantitative synthetic analysis brings interesting additional insight for reconciling features observed in historical, archaeomagnetic and paleomagnetic field models. In our simulations intense magnetic flux patches spend more time at the preferred locations assigned by the mantle heterogeneity than elsewhere, while being mobile, thus producing a reduced signature in the paleomagnetic field. In our models the probability of a patch to be near a preferred location (represented by p in Table 3) ranges ~10%–30%. Low probabilities occur when very weak convection results in weak mantle control or when very vigorous convection causes strong time dependence, while high probabilities (or partial locking) is favored for intermediate Ra numbers and when the boundary heterogeneity is enhanced. We therefore propose that the present intense geomagnetic flux patches are at their preferred locations due to a high probability, but that they often drifted in the past, thus producing a reduced signature in the paleomagnetic field. We note, however, that while the number of patches per snapshot varies with time, our models often exhibit snapshots with one patch per hemisphere, as opposed to the two patches prevailing in the current geomagnetic field.

[31] *Bloxham* [2002], inspired by earlier work of *Sarson et al.* [1997] who did not use a fully 3D dynamo model, already pointed out that imposing a Y_2^2 heat flux pattern on a numerical dynamo can lead to time-averaged magnetic flux patches comparable to those found in the paleomagnetic field, while patches exhibit significant mobility, with some periods characterized by less than two patches, and other periods with more than two patches. The present study concurs with that of *Bloxham* [2002] and provides a general framework for understanding the intriguing fact that the present locations of the high-latitude intense geomagnetic field patches are quite close to those tentatively found in models of the time-averaged field over the past few Myr [*Johnson and Constable*, 1995, 1997; *Kelly and Gubbins*, 1997] whereas the non-dipole field in most of those models is much weaker than the present non-dipole field [e.g., *Johnson and Constable*, 1995] and archaeomagnetic field models show that those patches have significantly migrated over the past 7000 years [*Korte and Constable*, 2005].

[32] Finally, our results also show that the time-averaged field displays weaker, and sometimes less, patches in the southern hemisphere than in the northern hemisphere. This we noted could be due to a stronger meridional shear in the mantle-driven zonal flow in the southern hemisphere, reducing the lifetime of intense patches there. If the mechanisms at work in our models are indeed reflected in the paleomagnetic field, it should have a weaker non-zonal signature in the southern hemisphere. However, current paleomagnetic field models do not have enough spatial resolution to confirm or dispute this result [*Johnson and McFadden*, 2007]. Future

improvements in modeling the geomagnetic field on various time scales and better understanding of the thermal heterogeneity of the lower mantle will shed more light on the behavior of intense geomagnetic flux patches and allow this scenario to be further tested.

References

Amit, H., and P. Olson (2004), Helical core flow from geomagnetic secular variation, *Phys. Earth Planet. Inter.*, *147*, 1–25, doi:10.1016/j.pepi.2004.02.006.

Amit, H., and P. Olson (2006), Time-average and time-dependent parts of core flow, *Phys. Earth Planet. Inter.*, *155*, 120–139, doi:10.1016/j.pepi.2005.10.006.

Amit, H., P. Olson, and U. Christensen (2007), Tests of core flow imaging methods with numerical dynamos, *Geophys. J. Int.*, *168*, 27–39, doi:10.1111/j.1365-246X.2006.03175.x.

Amit, H., J. Aubert, G. Hulot, and P. Olson (2008), A simple model for mantle-driven flow at the top of Earth's core, *Earth Planets Space*, *60*, 845–854.

Aubert, J. (2005), Steady zonal flows in spherical shell fluid dynamos, *J. Fluid Mech.*, *542*, 53–67, doi:10.1017/S0022112005006129.

Aubert, J., H. Amit, and G. Hulot (2007), Detecting thermal boundary control in surface flows from numerical dynamos, *Phys. Earth Planet. Inter.*, *160*, 143–156, doi:10.1016/j.pepi.2006.11.003.

Aubert, J., H. Amit, G. Hulot, and P. Olson (2008a), Thermo-chemical flows couple the Earth's inner core growth to mantle heterogeneity, *Nature*, *454*, 758–761, doi:10.1038/nature07109.

Aubert, J., J. Aurnou, and J. Wicht (2008b), The magnetic structure of convection-driven numerical dynamos, *Geophys. J. Int.*, *172*, 945–956, doi:10.1111/j.1365-246X.2007.03693.x.

Bloxham, J. (2002), Time-independent and time-dependent behaviour of high-latitude flux bundles at the core-mantle boundary, *Geophys. Res. Lett.*, *29*(18), 1854, doi:10.1029/2001GL014543.

Bloxham, J., and D. Gubbins (1987), Thermal core-mantle interactions, *Nature*, *325*, 511–513, doi:10.1038/325511a0.

Bloxham, J., and A. Jackson (1991), Fluid flow near the surface of the Earth's outer core, *Rev. Geophys.*, *29*, 97–120, doi:10.1029/90RG02470.

Carlut, J., and V. Courtillot (1998), How complex is the time-averaged geomagnetic field over the past 5 Myr?, *Geophys. J. Int.*, *134*, 527–544, doi:10.1046/j.1365-246x.1998.00577.x.

Christensen, U., and J. Aubert (2006), Scaling properties of convection-driven dynamos in rotating spherical shells and application to planetary magnetic fields, *Geophys. J. Int.*, *166*, 97–114, doi:10.1111/j.1365-246X.2006.03009.x.

Christensen, U., and P. Olson (2003), Secular variation in numerical geodynamo models with lateral variations of boundary heat flow, *Phys. Earth Planet. Inter.*, *138*, 39–54, doi:10.1016/S0031-9201(03)00064-5.

Christensen, U., P. Olson, and G. Glatzmaier (1999), Numerical modelling of the geodynamo: A systematic parameter study, *Geophys. J. Int.*, *138*, 393–409, doi:10.1046/j.1365-246X.1999.00886.x.

Glatzmaier, G. (2002), Geodynamo simulations: How realistic are they?, *Annu. Rev. Earth Planet. Sci. Lett.*, *30*, 237–257, doi:10.1146/annurev.earth.30.091201.140817.

Glatzmaier, G., R. Coe, L. Hongre, and P. Roberts (1999), The role of the Earth's mantle in controlling the frequency of geomagnetic reversals, *Nature*, *401*, 885–890, doi:10.1038/44776.

Gubbins, D., P. Willis, and B. Sreenivasan (2007), Correlation of Earth's magnetic field with lower mantle thermal and seismic structure, *Phys. Earth Planet. Inter.*, *162*, 256–260, doi:10.1016/j.pepi.2007.04.014.

Hulot, G., C. Eymin, B. Langlais, M. Mandea, and N. Olsen (2002), Small-scale structure of the geodynamo inferred from Oersted and Magsat satellite data, *Nature*, *416*, 620–623, doi:10.1038/416620a.

Jackson, A., A. Jonkers, and M. Walker (2000), Four centuries of geomagnetic secular variation from historical records, *Philos. Trans. R. Soc. London, Ser. A*, *358*, 957–990, doi:10.1098/rsta.2000.0569.

Johnson, C., and C. Constable (1995), The time averaged geomagnetic field as recorded by lava flows over the past 5 Myr, *Geophys. J. Int.*, *122*, 489–519, doi:10.1111/j.1365-246X.1995.tb07010.x.

Johnson, C., and C. Constable (1997), The time-averaged geomagnetic field: Global and regional biases for 0–5 Ma, *Geophys. J. Int.*, *131*, 643–666, doi:10.1111/j.1365-246X.1997.tb06604.x.

Johnson, C., and P. McFadden (2007), Time-averaged field and paleosecular variation, in *Treatise on Geophysics*, vol. 5, *Geomagnetism*, edited by M. Kono, pp. 417–453, Elsevier, Amsterdam.

Kelly, P., and D. Gubbins (1997), The geomagnetic field over the past 5 million years, *Geophys. J. Int.*, *128*, 315–330, doi:10.1111/j.1365-246X.1997.tb01557.x.

Khokhlov, A., G. Hulot, and J. Carlut (2001), Towards a self-consistent approach to palaeomagnetic field modelling, *Geophys. J. Int.*, *145*, 157–171, doi:10.1111/j.1365-246X.2001.01386.x.

Khokhlov, A., G. Hulot, and C. Bouligand (2006), Testing statistical palaeomagnetic field models against directional data affected by measurement errors, *Geophys. J. Int.*, *167*, 635–648, doi:10.1111/j.1365-246X.2006.03133.x.

Korte, M., and C. Constable (2005), Continuous geomagnetic models for the past 7 millennia ii: Cals7k, *Geochem. Geophys. Geosyst.*, *6*(2), Q02H16, doi:10.1029/2004GC000801.

Labrosse, S. (2002), Hotspots, mantle plumes and core heat loss, *Earth Planet. Sci. Lett.*, *199*, 147–156, doi:10.1016/S0012-821X(02)00537-X.

Masters, G., G. Laske, H. Bolton, and A. Dziewonski (2000), The relative behavior of shear velocity, bulk sound velocity, and compressional velocity in the mantle: Implications for chemical and thermal structure, in *Earth's Deep Interior*, *Geophys. Monogr. Ser.*, vol. 117, edited by S. Karato et al., AGU, Washington, D. C.

Olson, P., and U. Christensen (2002), The time averaged magnetic field in numerical dynamos with nonuniform boundary heat flow, *Geophys. J. Int.*, *151*, 809–823, doi:10.1046/j.1365-246X.2002.01818.x.

Olson, P., U. Christensen, and G. Glatzmaier (1999), Numerical modeling of the geodynamo: Mechanisms of field generation and equilibration, *J. Geophys. Res.*, *104*, 10,383–10,404, doi:10.1029/1999JB900013.

Olson, P., I. Sumita, and J. Aurnou (2002), Diffusive magnetic images of upwelling patterns in the core, *J. Geophys. Res.*, *107*(B12), 2348, doi:10.1029/2001JB000384.

Sarson, G., C. Jones, and A. Longbottom (1997), The influence of boundary region heterogeneities on the geodynamo, *Phys. Earth Planet. Inter.*, *101*, 13–32, doi:10.1016/S0031-9201(96)03248-7.

Secco, R., and H. Schloessin (1989), The electrical resistivity of solid and liquid Fe at pressures up to 7 GPa, *J. Geophys. Res.*, *94*, 5887–5894, doi:10.1029/JB094iB05p05887.

Sreenivasan, B., and D. Gubbins (2008), Dynamos with weakly convecting outer layers: Implications for core-mantle boundary interaction, *Geophys. Astrophys. Fluid Dyn.*, *102*, 395–407, doi:10.1080/03091920801900047.

Takahashi, F., H. Tsunakawa, M. Matsushima, N. Mochizuki, and Y. Honkura (2008), Effects of thermally heterogeneous structure in the lowermost mantle on the geomagnetic field strength, *Earth Planet. Sci. Lett.*, *272*, 738–746, doi:10.1016/j.epsl.2008.06.017.

Willis, P., B. Sreenivasan, and D. Gubbins (2007), Thermal core-mantle interaction: Exploring regimes for 'locked' dynamo action, *Phys. Earth Planet. Inter.*, *165*, 83–92, doi:10.1016/j.pepi.2007.08.002.

H. Amit, Laboratoire de Planétologie et de Géodynamique, UMR 6112, Université de Nantes, CNRS, Nantes Atlantiques Universités, 2 rue de la Houssinière, F-44000 Nantes, France. (Hagay.Amit@univ-nantes.fr)

J. Aubert, Equipe de Dynamique des Systèmes Géologiques, Institut de Physique du Globe de Paris, Université Paris-Diderot, INSU, CNRS, Case 89, F-75252 Paris, France.

G. Hulot, Equipe de Géomagnétisme, Institut de Physique du Globe de Paris, Université Paris-Diderot, INSU, CNRS, 4 Pl. Jussieu, F-75252 Paris CEDEX 05, France.